ANISOTROPIC STRUCTURE TO CONTROL PROPAGATION: SURFING LOAD EXPERIMENTS

Portions of this chapter contain content from "A non-constraining templated powder grid method for the measurement of strain" by N.R. Brodnik, C.-J. Hsueh, and M.T. Johnson, which was published in Strain in 2018 as well as from "Guiding and trapping cracks with compliant inclusions for enhancing toughness of brittle composite materials", which has been submitted to the Journal of Applied Mechanics.[1, 2] N.R. Brodnik led the design and fabrication of composite specimens for mechanical testing as well as the fabrication of grids for displacement measurement. C.-J. Hsueh led the numerical simulations for expected behavior as well as the design of the surfing load setup and the actual testing of specimens. Finally, G. De Luca is also acknowledged for his assistance in the evaluation of surfing load's suitability for the testing of ceramic systems. C.-J. Hsueh is also recognized for his assistance with the design of the simulation figures used in this work.

0.1 Introduction

The objective of this thesis work is to explore the effects of designed anisotropy on fracture properties and demonstrate how, alongside improved processing control, this anisotropic structure can improve the toughness of brittle composites. However, as was established in Chapter 1, formally characterizing the toughness of composite structures with arbitrary design is not straightforward, so careful consideration must be given to how structures are fabricated as well as how they are characterized. To address these issues, this chapter will explore how experimental design informed by numerical simulation can provide an avenue to investigate the influence of elastic contrast and anisotropic structure on fracture properties in heterogeneous composites.

The challenge of exploring fracture properties in composites with designed anisotropy arises from several different factors which must be addressed if experiments are to provide accurate data that is reflective of true material behavior. The two most significant of these factors are the location of crack-inclusion interaction events as well as the influence of elastic contrast on the strain field around the crack. The location of crack-inclusion interaction is crucial because, in the case of composite structures with discrete, macroscale inclusions with orientationally dependent design, the traditional assumption of effectively homogeneous behavior does not hold. Therefore, the location of the inclusions with respect to overall structure must be considered

during characterization. This point is particularly critical to emphasize, because it means that many of the traditional fracture characterization techniques such as compact tension, 3- and 4-point bending, and double cantilever beam testing are not feasible for evaluating the toughness of these composites, because they all rely on passive measurement of load and a particular specimen geometry for determination of fracture toughness. In cases of composites with microscale heterogeneities, this type of passive toughness characterization is still suitable so long as the spacing between heterogeneities is relatively small with respect to the size of the precrack. However, in the case of designed macroscopic inclusions and bulk composite structures, this is not the case. Consider a bimaterial beam being subjected to flexure with a single interface between the two materials that is parallel to the neutral axis of bending. If the only toughness enhancement exhibited by this composite structure is due to crack interaction with the bimaterial interface, the failure strength measured in bending will vary depending on the location of this interface with respect to the neutral axis, as shown in Figure 0.1. This variation in strength does not depend on the properties of the interface, but rather on the geometry of the specimen being tested. Logical extension of this idea clearly demonstrates how testing heterogeneous structures of arbitrary design is not sensible. For tests that determine toughness from measured strength, the strength will depend on the absolute position of the heterogeneity within the specimen, which means the test does not provide a meaningful evaluation of composite toughness as a material property. For this reason, in order to properly evaluate the toughness of composite structures with designed anisotropy, conditions of geometrically-independent, globally stable crack growth are required.

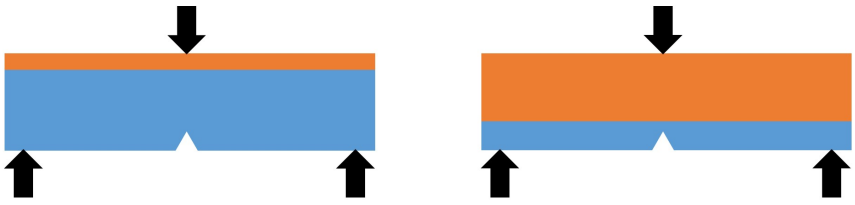

Figure 0.1: Schematic image of two bimaterial bend bars being subjected to 3-point bending. If toughening is achieved through property contrast between the two materials, these two bars will exhibit different strengths based solely on the location of the interface with respect to the neutral axis and precrack.

Beyond crack location dependence, the other challenge that must be addressed is the influence of elastic contrast on the stress field around the crack tip. In the

case of dissimilar materials, it has been demonstrated that elastic contrast can have an influence on crack behavior by means of residual stresses, and the ratios of relative stiffness have an influence on how the crack behaves and whether it will pass through the interface between the two materials or be trapped along it.[3] However, the presence of elastic contrast presents another issue, because any elastic contrast in the environment around the crack tip will influence the resultant crack tip stress field as well as the analogous displacement field. Because the crack tip stress field scales with $r^{-\frac{1}{2}}$, where r is the radial distance from the crack tip, it is expected that even inclusions that are appreciably far from the tip of the crack will influence its propagation behavior, albeit less than those closer to the crack.[4] This means that in order to properly evaluate the toughness of a crack propagating through a heterogeneous system, the toughness evaluation must account for all heterogeneities present within that system. Normally this problem is addressed by treating the heterogeneous structure as effectively continuous and homogeneous and evaluating the toughness of the composite structure as a singular material. This approach works well for heterogeneous microstructures, but is not well suited to macroscopic inclusions with arbitrary spatial position for reasons that have already been established.

These two challenges together limit the scope of tests that are well suited for the mechanical characterization of composite structures with macroscale anisotropic inclusions of arbitrary design and spacing. In order for a test to provide meaningful insight, it must provide stable growth of the crack throughout the test without the aid of specimen geometry (e.g. grooves, tapers, crack channels). Additionally, in any tests performed, the mechanical behavior of the entire composite structure must be evaluated rather than calculating toughness from a load or strength measurement for a specific specimen geometry. In the case of this investigation, these two issues were addressed through the surfing load testing design and J-integral calculation done using displacement maps produced with the grid method. These two techniques together were used to investigate parameterized composite structures with both isotropic and anisotropic inclusions.

0.2 Geometrically-Independent Stable Crack Growth: Surfing Load

It has been previously established that to properly characterize composite structures of arbitrary geometry, it is necessary to have crack growth that is stable throughout the entirety of mechanical testing and does not rely on any added specimen geometry to guide the crack. In this investigation, these requirements were achieved through

a configuration referred to as surfing load. The surfing load boundary condition is a specific macroscopic boundary condition for stable crack growth originally developed by B. Bourdin and demonstrated in M. Z. Hossain et al.[5] The idea behind this boundary condition is to prescribe a Mode I opening displacement field that is localized to the area around the crack. This Mode I field is sufficiently large to propagate the crack, but there is no tensile displacement applied well in front of the crack, such that crack propagation is limited by the region over which this opening field exists. This opening field is then prescribed to travel at a steady velocity from one side of the specimen to the other. As this opening field moves, tensile stresses move along the specimen, making it energetically favorable for the crack to propagate at the same rate as the velocity of these tensile stresses. The theoretical approach for applying this type of boundary condition is discussed in detail in Hossain et al. and in the thesis of C.-J. Hsueh.[5, 6]

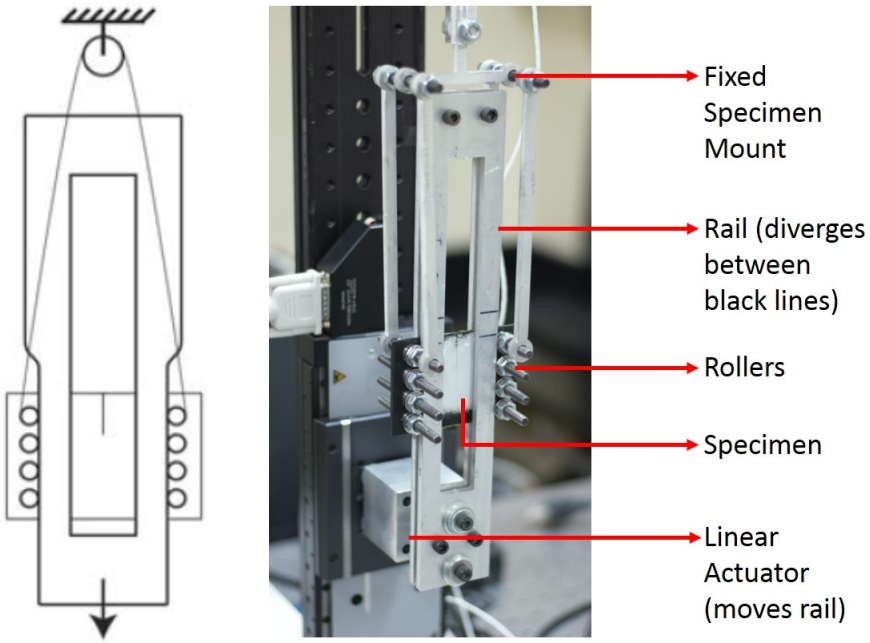

(a) Schematic Image (b) Experimental Setup

Figure 0.2: Schematic image of the surfing load design and a photograph of the analogous experimental setup. The black lines on the photographed rail surround the region of rail width divergence, which is significantly exaggerated in the schematic.

Applying this type of boundary condition is ideal for creating stable crack growth under tensile loading, as the rate of crack propagation is directly correlated with the velocity prescribed in the boundary condition. However, applying a load with this degree of complexity in an experimental environment requires careful design. To

address this, Hsueh, Bhattacharya, and Ravichandran developed a loading apparatus that can apply a boundary condition to physical samples that is very similar to the surfing load condition. A schematic of this design is shown in Figure 0.2a and the experimental equivalent is shown in Figure 0.2b. A stiff metal rail with a width increase along its outside edge is used to apply the Mode I load to the specimen during testing. This width increase is chosen to be exactly equal to the opening displacement needed to propagate a crack through the specimen. The outside edges of the specimen are constrained to the profile of the rail using a series of stiff pins surrounded by bushings and roller bearings. These pins pass through the specimen such that when the metal rail forces them outward, they pull on the material that surrounds them, forcing it open. Because the pins are kept flush to the rail and hold the sample in place, the surfing load profile is dictated by the taper along the outside of the rail, and the velocity of the Mode I opening regime is set by the velocity of the rail with respect to the sample. The number of pins chosen to apply the load was a balance between applying the surfing load as smoothly as possible and having the load fixture be stiff with respect to the specimen. In Figure 0.2, a total of 8 pins are shown passing through the specimen (4 on each side), as these were the smallest pins that were able to load the sample without flexing. In this load configuration, stable crack growth is actually maintained through the controlled failure of the specimen. The opening displacement on the outside edge of the rail is chosen to be sufficiently large to crack the specimen, and once the crack propagates due to this displacement the load drop associated with propagation is significant enough to prevent unstable crack growth.

0.3 Sample Design

0.3.1 Specimen Fabrication

The samples used in the surfing load design present some challenges from a fabrication standpoint, as they require arrays of holes on either end of the sample through which pins can be inserted to apply the surfing load. To address this, all samples investigated in this study were fabricated using digital light processing on an Autodesk Ember 3D Printer (Autodesk, San Rafael, CA). All specimens were printed using either a clear system known as PR48 or a black system known as PR57-K. Both polymers are urethane acrylate photopolymer blends with comparable stiffnesses and strengths. The formula for PR48 is reported in reference [7] and the formula for PR57-K is a modification of the PR48 formulation that introduces black dyes for color and opacity. Using either polymer, the Autodesk Ember has a print voxel size of 50 x

50 x 50 microns which is well suited to printing surfing load specimens with high fidelity. The design for the surfing load specimens is shown in Figure 0.3. Surfing load specimens were printed to be 90 mm x 64 mm by 2.5 mm, with some additional thickness reinforcement present around the pinholes.

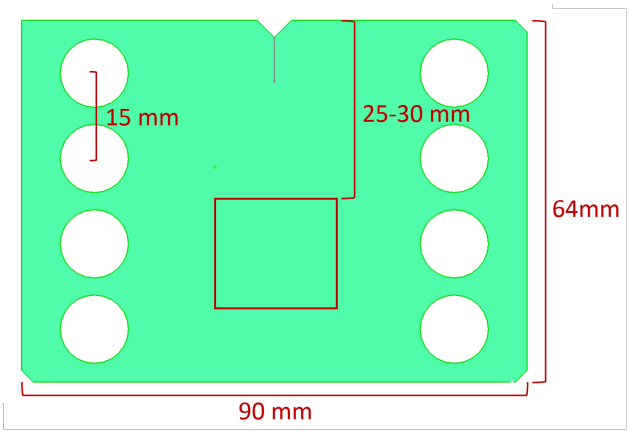

Figure 0.3: Schematic design of a surfing load specimen. Red box indicates region in which heterogeneous structures were analyzed.

It should also be noted that as previously discussed, in order for toughness characterization of heterogeneous structures to be reflective of behavior of the entire structure, all of the composite designs investigated in this study contained a relative small number of inclusions confined to a single region of characterization. This region of analysis is shown in the red box in Figure 0.3, which was placed between 25 and 30 mm down on the sample to allow for crack propagation to be fully stable before the start of analysis. Beyond this region, the sample was kept as homogeneous photopolymer. This allowed for uniform evaluation of crack interactions with inclusions and helped prevent any characterization bias that might arise due to the location of the crack with respect to the inclusions in the greater structure.

0.3.2 Composite Design

Once methods have been developed for continuous stable crack growth, the next step is to establish how the composite design space is going to be explored. This presents a particular challenge in the context of 3D printed composites because the design space is extremely large. To illustrate this point, traditional ceramic or metallic material design might use a parameter like volume fraction when describing the quantity of inclusions, dispersoids, pores, or toughening phases present in a particular composite design. This volume fraction, along with a description of the size and structure of the inclusions as well as the assumption that the inclusion phase is randomly

distributed, gives a clear description of heterogeneous structure within a particular composite. However, because processing techniques like additive manufacturing allow for control of the exact location of inclusions, volume fraction quickly becomes an inadequate descriptor, as there are effectively an infinite number of configurations of inclusions within a bulk structure, both uniform and nonuniform, that all have the exact same bulk volume fraction. This same principle holds with inclusion structure. In conventional composite theory, the influence of both structure and spacing of inclusions on fracture behavior has been explored for the most common inclusion shapes, including rods, spheres, and plates.[8] However, now that inclusions can be readily designed to be any shape or structure, exploring the space of possible inclusion shapes is not straightforward. Even when the the influence of inclusion shape is well understood, changes in material properties, including both stiffness and toughness, can have a dramatic effect on the behavior of the crack as it interacts with the inclusion as well as whether or not the crack becomes pinned at the interface between materials. All of these factors together make the design space for composites with designed anisotropic structures very large.

To better constrain the design space, we took the approach of parameterizing the composite structure to constrain as many geometric and material properties as was possible. Previously, layered printed structures were explored in double cantilever beam testing, but all structure and geometry in this study were effectively constrained to one dimension.[9] We chose to investigate arrays of circular inclusions in a staggered square pattern, as shown in Figure 0.4a. The inclusions were chosen to have a fixed spacing both between inclusions as well as between successive rows. The spacing d was chosen to be either 5 or 8 mm, depending on number of inclusions being included in the region of interest. Within this fixed spacing, the inclusion radius was varied to change the effective properties of the composite structure while maintaining a relatively standardized design.

In addition to a fixed arrangement with variable radius, a method was needed to vary the material properties without having unintended interfacial interactions or material incompatabilities. The main interest in this study was to explore elastic contrast, so, to provide a change in elastic contrast without creating unwanted incompatibility, the thickness of the printed material was changed at the inclusion locations, as shown in Figure 0.4b. This allows the whole composite to be printed from the same photopolymer. Printed samples were 2.5 mm thick, which is sufficiently thin to prevent any unwanted bending moments due to this thickness variation, and inclusion

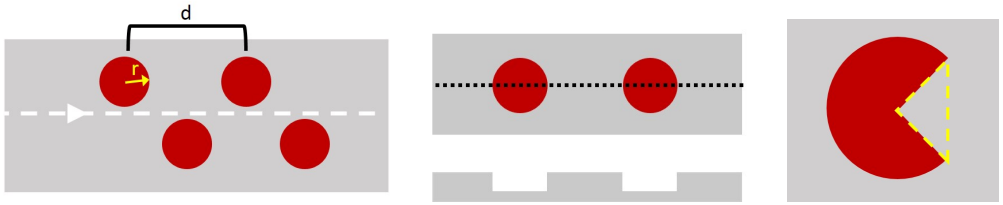

(a) Inclusion arrangment (b) Inclusion cross-section (c) Anisotropic Inclusion (right facing)

Figure 0.4: Schematic images of the parameterized composite design investigated in this study. Schematics show inclusion arrangement (a), inclusion thickness (b), and introduction of anisotropy (c). Anistropic inclusion is described as right facing to clarify directionality with respect to crack.

thickness was made to be 1/5 that of sample thickness. The inclusion and matrix layers were also made flush with one another on one side of the sample, as shown in Figure 0.4b to provide a single planar face for displacement mapping with the grid method. The change in thickness contrast has several effects on the relative properties of the photopolymer material. The first effect is the aforementioned reduction in effective inclusion stiffness, which is described in Equation 1

$$E^{inc} \propto \frac{t^{inclusion}}{t^{matrix}} \tag{1}$$

where E^{inc} is the effective elastic modulus of the inclusion with respect to the matrix, σ is the stress resulting from applied far field load, ϵ is strain, t^{matrix} is matrix material thickness, and $t^{inclusion}$ is inclusion thickness. Note that this is not an actual change in material properties, as the photopolymer material has a stiffness of about 740 MPa.[10] However, because the thinner inclusion regions are being characterized with respect to the thicker matrix regions, and they are both being subjected to the same far-field-loading, the inclusions will experience 5 times greater stress for the same loading. Consequently, they will effectively behave as though they have 1/5 the stiffness of the surrounding matrix. This same principle applies to effective inclusion toughness, as shown in Equation 2

$$\mathcal{G}_c^{inc} = \frac{(K_{Ic}^{inc})^2}{E^{inc}} \propto \frac{t^{inclusion}}{t^{matrix}} \tag{2}$$

where $\mathcal{G}_c^{inc}$ is the effective critical strain energy release rate and K_{Ic} is the effective fracture toughness of the inclusion with respect to the matrix. Again, similar to

the stiffness, no material properties are actually changing, but because thickness variation changes the stress response to equivalent far-field loading, the relative toughnesses of the inclusion and matrix are different with respect to one another. Once the effective modulus and toughness of the inclusions are determined, these values can be incorporated into the composite design for a given geometry and unit cell arrangement. From here, the effective elastic modulus of the composite E^{eff} can be determined using a fast Fourier transform (FFT) calculation, and the effective strain energy release rate of the composite $\mathcal{G}_c^{eff}$ can be determined from the macroscopic J-integral. [6, 11–13]

Finally, once the inclusion arrangement, size, and properties have all been parameterized or constrained, the only remaining point of interest is the introduction of anisotropy. Because isotropic inclusions were chosen to be circles, anisotropy was introduced by cutting an isosceles right triangle out of the middle of the circle, to create an inclusion with directional stress concentrators as shown in Figure 0.4c. This allows for use of the same parameterization by circle radius and spacing for both isotropic and anisotropic inclusions and provides a reasonable basis of comparison.

0.4 Measurement of Toughness

0.4.1 Displacement Fields with Grid Method

With the surfing load method to provide stable crack growth in designed composite specimens, the next step in properly characterizing designed heterogeneous structures is developing a method of toughness evaluation that is not dependent upon the design parameters of the composite structure. As was established in Chapter 1, the J-integral developed by Rice is a promising candidate, as it provides a mathematically robust method for measuring toughness in a system and is able to capture changes in toughness that arise due to crack interactions with inclusions or other material contrast.[14] This J-integral technique is also able to measure changes in toughness as the crack propagates over time, as it does not rely on indirect strength measurements. However, in order to properly calculate the J-integral, full-field displacement measurements that do not affect mechanical response are needed throughout the fracture process.

Various types of non-contact full-field measurement methods have been implemented in experimental mechanics for well over 50 years and have proven to be extremely useful in the characterization of material behavior. Generally, these full-field measurement techniques can be divided into two categories: interferometric techniques

and geometric techniques. The former relies on interference patterns formed between a coherent light source interacting with the sample and a coherent reference light source, such as electronic speckle pattern, shearing, and moiré interferometry.[15] Interferometers can be used to track displacement along a single axis at sub-nanometer resolutions, but interferometric methods for measuring full-field displacements typically involve either a patterned surface, an intentionally roughened surface, or a material with particular optical properties, so resolutions tend to be limited to sub-micron or micron scales and only certain systems can be studied.[16–19] Although interferometric techniques can provide exceptionally high measurement resolution, even the simplest of interferometer setups is complex and sensitive to environmental effects such as vibration and sample drift, both of which are difficult to prevent in more complex setups such as the surfing load configuration.[20–23] Furthermore, displacements in interferometric techniques are deduced from measured interference patterns, so any error or experimental bias is not easily distinguished from measurement and must be carefully accounted for.[15, 16]

However, geometric techniques such as image correlation, speckle photography, digital image correlation (DIC), geometric moiré, and the grid method provide alternatives to interference-based measurement that are typically lower in accuracy, but are much more straightforward to implement and are not limited by the optical properties of the material. Of these, digital image correlation has gained particular popularity because of its simple implementation, especially compared to interferometric measurement techniques.[24, 25] Creating a pattern for DIC is very straightforward because only a random pattern of speckles is required. However, this random pattern can be optimized based on many different metrics, and the imaging analysis of these speckles can be done with a variety of methods.[21, 25–27] However, DIC does have some limitations, namely that resolution issues can be encountered when analyzing deformations that are both small and non-uniform, which are common in the fracture of brittle materials.[22] When addressing this issue, another non-interferometric technique known as the grid method acts as a compromise, in that it provides consistent measurement resolution of small and inhomogeneous strain while being relatively simple to implement.[28] The grid method is similar to DIC in that it is correlation based, however instead of using random patterns, it requires regular patterns of a known phase and pitch. By extracting the phase distributions of these regular patterns, a deformation field can be obtained. The improved nonlinear resolution of the grid method and its robustness against noise are particularly useful in characterizing brittle fracture, as deformation

during fracture is highly non-uniform and toughness calculations from full-field displacement measurements are very sensitive to noise. Introductions of numerical noise in amounts as small as 1% in DIC measurements have been shown to increase J-integral error by over 50%.[29]

The major disadvantage of the grid method compared to DIC is that the grid method relies on the deposition of a highly uniform and regular pattern as opposed to a random one.[30, 31] Some of the earliest grid mounting methods marked macro-scale grids onto samples and used the intersection points formed by the grid to track large scale displacements, such as those seen in sheet metal forming. [30, 32, 33] Macro-scale grids with pitches on the order of 0.8-1 mm have also been produced by spraying paint through a stencil.[34, 35] On the opposite end of the size spectrum, the smallest grids that have been used for full field strain analysis are sub-nanometer grids formed by the atoms in the material itself and imaged using high-resolution electron microscopy and atomic force microscopy.[36–39]

For fracture of macro-scale brittle polymer specimens such as those being considered in this study, the grids of interest have pitches somewhere between the atomic scale and the macro scale, specifically on the order of 5-150 μm. These grids are typically produced by first printing a grid with either high resolution digital printing or metal halide printing onto a polymeric substrate and then transferring the print layer from this substrate onto the sample using an adhesive such as epoxy.[40] This technique has the advantage that it can rely on high-fidelity printing techniques to produce uniform grids, and it has already been used to characterize the fracture of relatively high-toughness materials such as aluminum.[41] However, when the material being fractured has a toughness or stiffness that is very low compared to the grid itself, the epoxy layer used to adhere the grid and the print layer of the grid itself can distort the displacement information such that the displacements observed optically do not reflect the actual deformation of the specimen. This type of distortion in low toughness specimens is not surprising when one considers the sample to be a layered structure composed of the material of interest, the epoxy, and the grid print layer. Distortions of similar nature have been reported due to strain limitations in the grid layer when grids are produced using decal paper.[28, 42]

The specimens of interest in this study were made of stereolithographically printed photopolymer PR48 [7], which is a blend of multifunctional acrylate precursors. This polymer has a modulus of about 740 MPa and a fracture toughness of about 0.2 MPa$\sqrt{\text{m}}$, giving it both low stiffness and toughness.[10, 43] This presents serious

concern when mounting grid patterns using traditional epoxy mounting methods, as both the epoxy and polymer grid layers themselves can make non-negligible contributions to the effective stiffness and toughness of the specimen, distorting results, as shown in Figure 0.5.

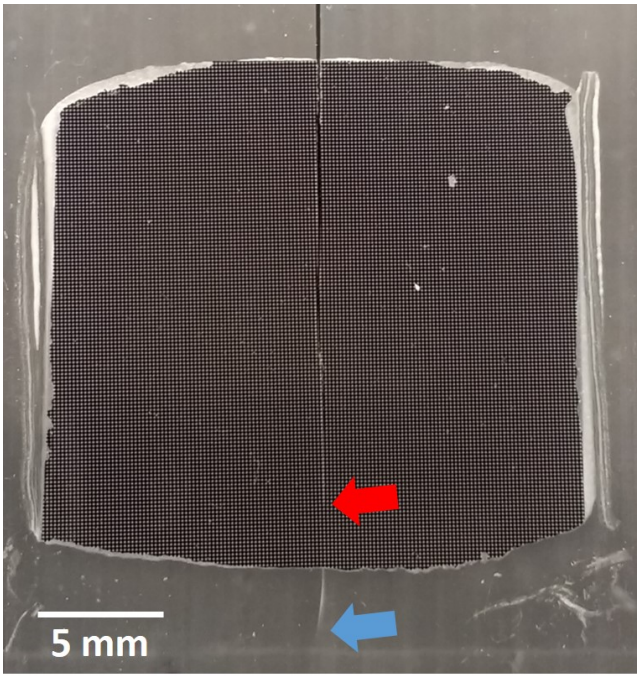

Figure 0.5: Closeup view of the region of interest on a transparent PR48 sample, with an epoxy grid mounted on the front face. Note that the presence of the grid toughens the front of the specimen so that the crack on the front side (red arrow) has not propagated as far as the crack on the backside (blue arrow), which is visible through the transparent polymer.

To limit this distortion, a new grid mounting method was developed that is suitable for displacement and fracture studies with any system compatible with photosensitive acrylic polymer. These new grids are formed by making a textured pattern of the grid on the specimen using photopolymer and then filling the spaces in this textured pattern with opaque powder pigment to achieve the needed contrast for grid method. The advantage of this implementation is that there is no need for a cured epoxy layer to create the grid pattern. Therefore, the bias of the epoxy layer is eliminated, and sample processing time is greatly reduced.

0.4.2 Powder Grid Method

The templates for the textured photopolymer grid pattern were made using traditional semiconductor photolithography techniques. A silicon wafer was coated with SU-8

photoresist to a thickness of 50-70 μm and then exposed through a square grid-patterned mask and subsequently developed. The result of this is a silicon wafer which has a uniform pattern of SU-8 pillars that are 50-70 μm tall and have spacing corresponding to the pitch of the grid. This resist-patterned wafer is then coated with Sylgard 184 liquid silicone and placed under rough vacuum for 30 min to allow for proper infiltration and degassing. Once infiltration is sufficient such that all trapped air is removed, the silicone is cured for 2 hr at 70 °C. Once fully cured, the silicone is separated from the resist-coated wafer to produce a silicone template mold with uniform square channels 50-70 μm deep with a pitch matching that of the silicon wafer. In this study, the grid pitch was chosen to be 120 μm based on the specifications of the camera used for imaging, but this pitch can be adjusted to be smaller or larger depending on the needs of the imaging setup.

To transfer a grid pattern onto a sample, a layer of liquid photopolymer is deposited onto the sample of interest using a transfer pipette. The photopolymers used in this study were PR48 and PR57-Y (Autodesk, San Rafael, CA). The silicone grid template is then introduced onto the liquid layer and allowed to settle under its own weight, after which the sample and silicone template are placed under rough vacuum for 10 minutes to remove all trapped air. After this rough vacuum, the samples are removed from the chamber, and any excess photopolymer is removed from around the sides of the template. The sample is then placed under UV light for 14-30 min (depending on sample thickness) to fully cure the liquid PR48 polymer into the shape of the silicone template. Because the polymer is physically constrained by the shape of the template, overexposure causing distortion of the grid pattern is not of particular concern. However, if the samples are placed in the UV oven for too long, the template can become difficult to remove from the sample, which can lead to the damage. Once polymerized, the photopolymer preferentially adheres to the specimen instead of the silicone template, so the template can be easily removed for repeated use. Once separated, both the sample and template are cleaned with isopropanol.

At this point, the surface of the sample is covered in a uniform array of pillars which correspond to the grid template, but this grid pattern has no optical contrast. To add optical contrast, the valleys between these pillars are filled with an opaque powder that is optically differentiable from the grid material. In the case of this study, the photopolymer used was translucent, so the powder chosen to fill in the valleys was Al_2O_3 with a median particle size of 350 nm (Baikowski Malakoff HP DPM [44]). The powder is either physically agitated or ground in a mortar and pestle to break up

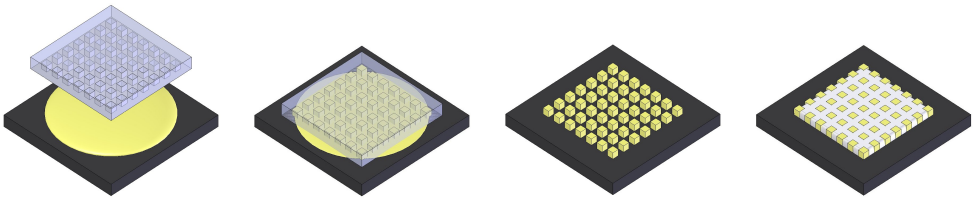

(a) Photopolymer deposition (b) Placement of template (c) UV cure/template removal (d) Powder fill-in

Figure 0.6: A schematic of the grid mounting process, shown with yellow photopolymer for clarity.

any aggregated particles and is then spread over the patterned sample face using a straight edge, taking care not to damage the array of pillars, as this will disrupt the grid regularity. Once the powder is spread, this same flat edge is used to remove any excess powder, leaving a grid pattern of white alumina on the sample. A schematic of the full process is shown in Figure 0.6.

Because the grid method only relies on the pitch and frequency of the waveform created by the applied grid, the color contrast of the grid can be varied based on the the color of the sample itself. Samples investigated in this study were either transparent or dark in color, and white powder was used to make the grid, but if a sample is brightly colored or white, a dark pigmented powder can be used to create a grid of black lines on the sample with no change in the efficacy of the grid. However, it is recommended that the powder chosen be neither carbon based nor a powder that would commonly be incorporated into lubricants, as these powders tend to smear during the spreading process, dramatically reducing imaging contrast. From a preparation time standpoint, fabrication of silicone templates for use in this method takes several hours, but templates are suitable for repeated use. Once templates are produced, the entire grid preparation process takes approximately one hour, far shorter than the epoxy cure step for traditional lithography grids, which can range from several hours to one day, depending on the epoxy.

0.4.3 Verification of Powder Grid Functionality

To ensure this new grid mounting method was comparable to prior grid methods and did not introduce any additional bias, some proof-of-concept testing was done to verify the functionality of these grids in controlled systems with well understood behavior. First, some synthetic testing was performed using images of grids. These images were digitally manipulated to simulate known amounts of translation and biaxial strain, and these modified images were then evaluated using the grid method

developed by Grédiac.[28] The results from the grid method measurements were then compared with the known values to ensure good fidelity. For these synthetic tests, three different grid types were compared: the powder grid developed for this investigation, a lithographically printed grid that would be used in conventional epoxy-mounted grid testing, and an idealized grid made using a superposition of two sine functions that was displayed as an intensity map. This last grid was only used for synthetic tests because it was produced digitally and does not exist in any physical form. The mathematical details of both fabrication of the digital grids as well as mathematical analysis of grid performance can be found in reference.[1] All three grids are shown in Figure 0.7.

The mean errors measured in pixels for both the biaxial strain and translation synthetic tests are shown in Figure 0.8. The fluctuating behavior seen in the translation error is a product of error arising from subpixel interpolation, and the variation in the digital grids results from aliasing effects due to imperfect subpixel interpolations of the perfect sinusoidal waves. When the three different grids are compared, the general trend is that the powder grid performs slightly worse than the lithographic and digital grids, but this is to be expected, as the powder grids themselves are fabricated using a lithographic grid as a starting template, and the fabrication process is expected to produce some additional error. However, this increase in error is still relatively small and is seen as a reasonable tradeoff to permit the use of the grid method in the fracture analysis of low toughness materials.

To verify the functionality of this new grid method in fracture studies, homogeneous PR48 specimens were fractured using the surfing load condition and characterized using the powder grid method. These specimens, which had a fracture region with dimensions of 62 mm x 36.5 mm x 1.5 mm, were printed using the same digital light processing techniques as the other surfing load samples (Ember® 3D Printer by Autodesk, San Rafael California). The powder grids developed were used to measure the displacement and strain fields, and the J-integral was then calculated from the strain field to determine the critical stress intensity factor. The stress intensity factors associated with different crack lengths are plotted in Figure 0.9. The measured critical stress intensity factor of the 3D printed polymer specimen was determined to be 0.187 ± 0.014 MPa$\sqrt{\text{m}}$. This is very similar to the previously measured value of 2 MPA$\sqrt{\text{m}}$, which both verifies the functionality of the powder grids as well as provides a suitable baseline of homogeneous photopolymer toughness for later experiments.

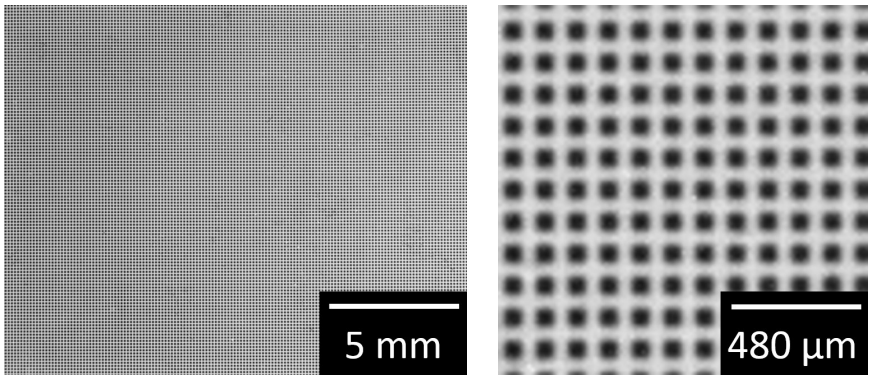

(a) Powder grids (b) Powder grids (magnified)

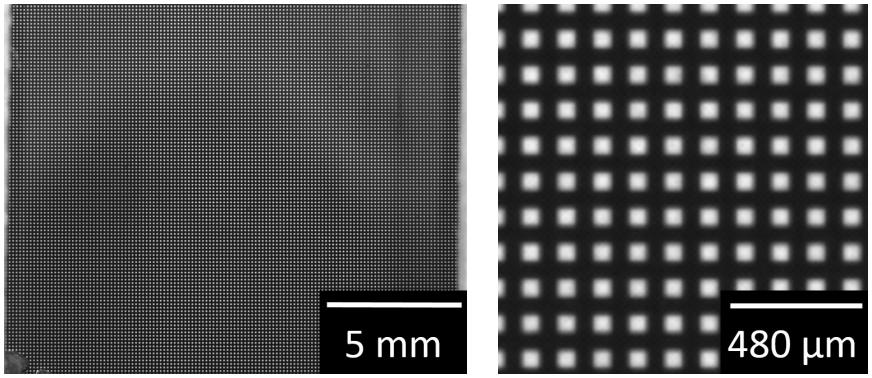

(c) Lithographic grids (d) Lithographic grids (magnified)

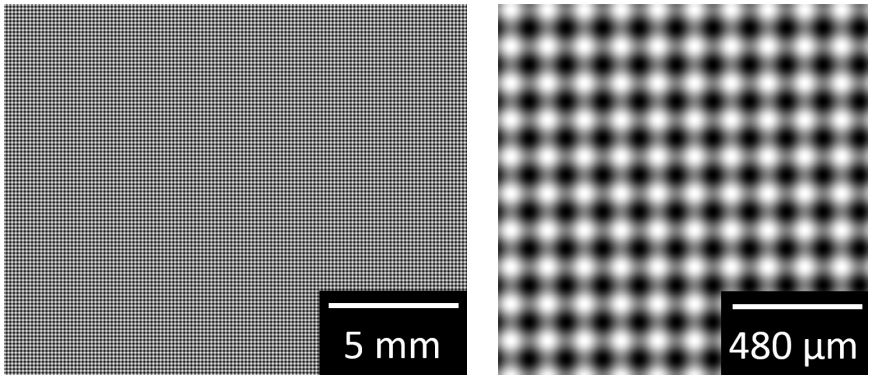

(e) Digital grids (f) Digital grids (magnified)

Figure 0.7: Grid patterns used in synthetic testing.

0.5 Results and Discussion

0.5.1 Numerical Simulations

With a means of fabricating and characterizing parameterized heterogeneous structures fully available, simulations of surfing load conditions were used to explore the design space in the context of effective stiffness and effective toughness. Simulations were done using the variational phase field models implemented by Bourdin.[45–47]

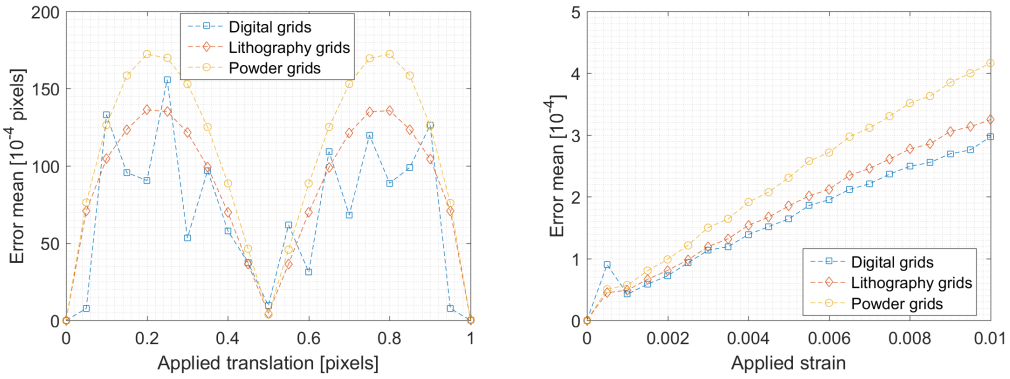

Figure 0.8: Mean errors measured from the synthetic translation and biaxial strain tests.

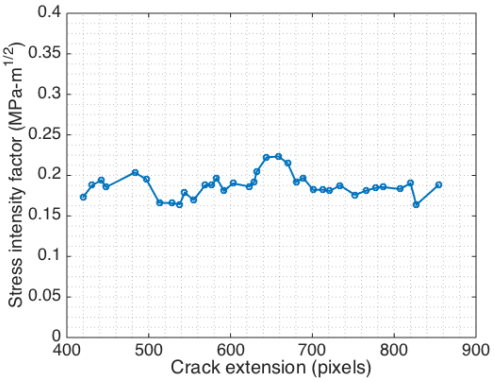

Figure 0.9: Stress intensity factor vs. crack extension for PR48 photopolymer in surfing load fracture conditions.

For the same pattern of staggered circles discussed in Section 0.3.2, the radius of the inclusions was changed and the effective stiffness of the system was measured numerically. Then, the effective toughness was measured numerically using surfing load conditions, and the two were plotted against one another, as shown in Figure 0.10. The numerical implementation of this simulation was done by C.-J. Hsueh and is discussed in reference.[6]

It is important to note that because the composite structures contain macroscopic discrete inclusions, the toughness is not necessarily uniform throughout the entire structure. However, extension of tradition fracture theory indicates that it is reasonable to assume that the effective toughness of the composite structure is the peak value of the J-integral, which is related to the peak strain energy release rate.[14, 48, 49] Because there was particular interest in the effect of elastic contrast on effective toughness, initial simulations were done without any toughness contrast between

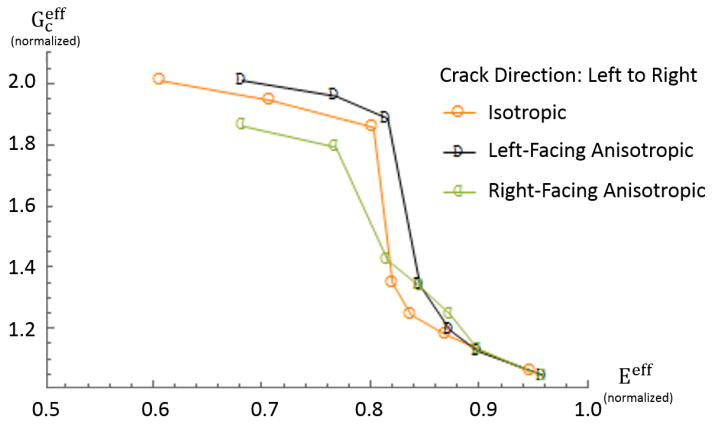

Figure 0.10: Comparison of effective stiffness and effective toughness (normalized to the matrix material) for composite structures with staggered patterns of either circular inclusions or anisotropic circular inclusions. For all cases, $E^{inclusion} = \frac{1}{5}E^{matrix}$. Crack propagation is described as left-to-right to establish directional distinction between different anisotropic inclusions.

the inclusions and matrix, so the only difference between the inclusion phase and matrix phase was elastic modulus, with inclusions be 1/5 as stiff as the matrix. Using this basis, the size of the inclusions was varied to change effective stiffness, and the impact on toughness was measured through the J-integral.

When explored in terms of effective stiffness, Figure 0.10 shows several interesting relationships. At the far right of the stiffness axis is the homogeneous matrix material, which has a normalized stiffness of 1 and a normalized toughness of 1. Once inclusions are introduced, the toughness increases slightly at the expense of stiffness. This increase is not actually due to direct interaction between the cracks and inclusions, but rather deflection of the crack due to attraction towards the more compliant heterogeneities. However, once inclusions are sufficiently large that $E^{Eff} \leq 0.8$ for the isotropic case, the crack is drawn into the inclusions and is pinned by the elastic contrast between inclusion and matrix. It should be noted that in the case of the simulation, the both the inclusions and matrix are treated as homogeneous materials with uniform unit thickness, so the observed toughening is due entirely to this elastic contrast effect. This phenomenon of crack pinning at the interface where there is an increase in elastic contrast causes a dramatic increase in the effective toughness of the composite structure, and is responsible for the jump in composite toughness.

The introduction of anisotropy has two distinct effects on the toughenss-stiffness

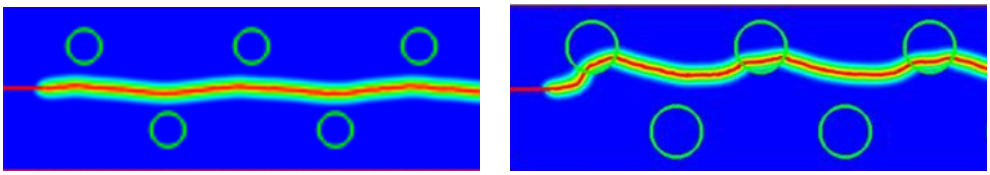

(a) Smaller inclusions (crack deflection) (b) Larger inclusions (crack pinning)

Figure 0.11: Simulations showing crack behavior with smaller and larger isotropic inclusions. For the smaller inclusions (a), $E^{Eff} = 0.95$, and only crack deflection is observed, which produces marginal toughness increase. For the larger inclusions (b) $E^{Eff} = 0.8$, and crack pinning is observed, which produces greater toughness increase.

relationship, namely it changes both the magnitude and location of the toughness increase due to crack pinning interactions. The change in magnitude of the toughness increase is directly related to the shape of the anisotropic inclusions, namely the the location of stress concentrators. For a crack that is traveling from left to right, a left facing anisotropic inclusion forces the crack to enter and exit the inclusion along the circular edge, so it effectively behaves like a circular inclusion, as shown in Figure 0.12a. For the right facing inclusions however, the stress concentrators in the inclusions make it far easier for the crack to exit the inclusion, as shown in Figure 0.12b, so the toughness improvement is not as significant in this case.

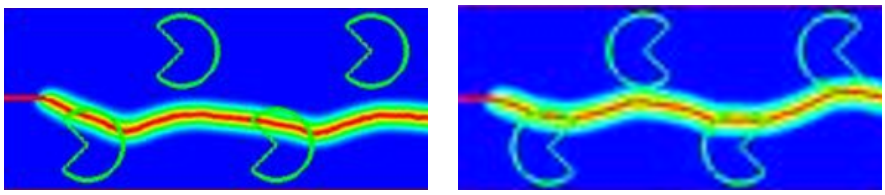

(a) Left Facing (b) Right Facing

Figure 0.12: Simulations showing effect of anisotropy on fracture. In both simulations, crack propagation is from left to right. Right facing inclusions (a) showed comparable toughness to isotropic inclusions, albeit at higher effective stiffness. Left facing inclusions (b) showed lower toughness than isotropic due to the presence of stress concentrators.

While the effect of anisotropy on the magnitude of the toughness increase is relatively straightforward, its effect on the location of the transition between crack deflection and elastic contrast crack pinning behavior is a bit more subtle, and arises due volume fraction effects. Because the anisotropic inclusions have a triangular section cut out of a circle of fixed radius, anisotropic inclusions have a smaller volume fraction of inclusion phase than isotropic inclusions of equivalent circle radius. Since effective

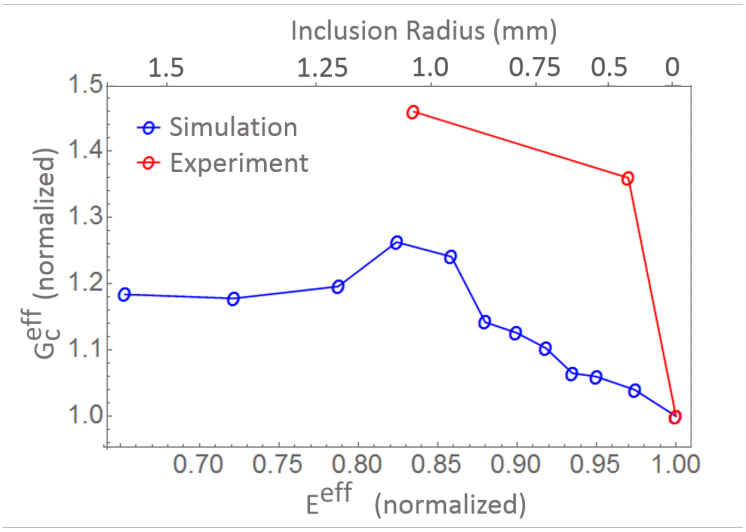

Figure 0.13: Comparison of effective stiffness and effective strength (normalized to the matrix material) for composite structures with staggered patterns off isotropic circular inclusions made by varying sample thickness. Comparison shows both expected toughness from simulation as well as toughness measured in experiment.

stiffness is determined by the volume fraction of compliant inclusion phase, the anisotropic inclusions can achieve elastic contrast crack pinning behavior with a smaller reduction in effective stiffness.

0.5.2 Experimental Results

In the experiments on PR48 and PR57-K, inclusions had a lower effective stiffness, similar to simulations, but also a lower effective toughness than the surrounding matrix, so analysis of behavior was not as straightforward. Even in this case however, the toughness of the composite can still be characterized using a J-integral with displacement maps from the powder gird method.

Initial experimental characterization focused solely on isotropic inclusions in an attempt to capture both deflection and elastic contrast pinning behavior as inclusion size varied. To have a more complete understanding of expected behavior, additional simulations were also carried out with inclusions that had both lower stiffness and lower toughness. A comparison between simulation and experimental results is shown in Figure 0.13.

Observation of Figure 0.13 shows several apparent differences between simulation and experiment. The most apparent difference between simulation and experiment in Figure 0.13 is that for all cases, the toughness measured in experiment is markedly

higher than the toughness predicted by simulation. It is suspected that this difference arises not from inaccuracies in the simulation, but rather from unexpected behaviors arising from sample design. Changes in thickness proved to be a convenient way of introducing elastic contrast without a distinct material interface, but these thickness changes also created unintended geometric effects.

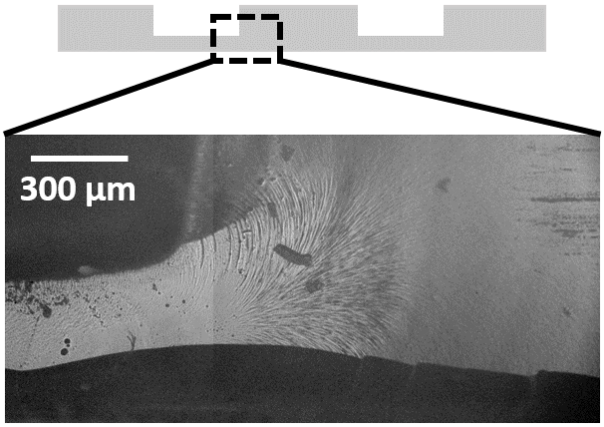

Figure 0.14: Optical micrograph showing the unintended geometrical toughening effect in the $E^{Eff} = 0.83$ sample. Because elastic contrast was introduced through thickness variation, the crack was forced to bow outward around the thickness change when exiting the inclusion, creating additional toughening.

When the crack becomes pinned in the more compliant inclusions, the change in thickness also causes a reduction in crack front length. Then, when the crack reaches the end of the inclusion and propagates back into the matrix, the pinned crack front is forced to bow due to the change in geometry in order to continue propagation into the thicker matrix, evidence of which is shown in Figure 0.14. This added geometrical bowing effect causes additional toughening beyond what would be present if the inclusions were instead the same thickness as the matrix, but a different material.

In addition to this geometric effect, there is another disparity between simulation and experiment. In the case of small inclusions where effective stiffness is higher, the toughness measured in experiment is substantially higher than predicted by simulation, with the gap between simulation and experiment being far greater than for larger inclusions. This additional disparity arises because at small inclusion sizes, simulation predicts that the crack will exhibit only a slight deflection behavior, where it is briefly drawn toward the inclusions, but never pinned by them. However, in actual experiments, the crack was reliably pinned by inclusions regardless of size, which leads to the significantly higher toughness seen at high effective stiffness

in Figure 0.13. The main cause of this difference in behavior is crack alignment. In simulation, it is straightforward to center the crack perfectly between rows of inclusions in the composite structure such that is deflects evenly as it propagates. However, doing this in experiment is not as simple. An example of this is shown in Figure 0.15, where a difference in crack position of about 300 μm is enough to produce an elastic contrast crack pinning event. This level of sensitivity to small deviations in crack position is likely why no experimental specimens exhibited crack deflection behavior without also having elastic contrast pinning.

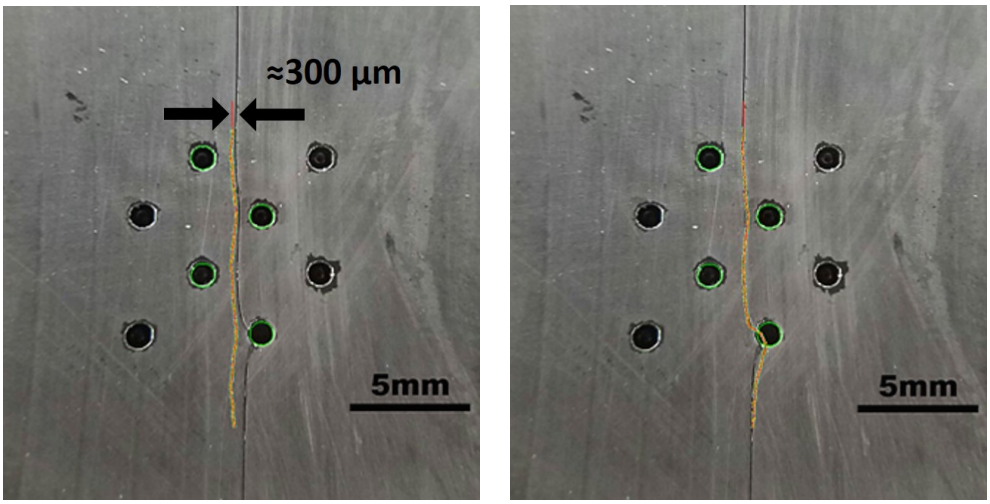

(a) Crack and simulation not aligned (b) Crack and simulation aligned

Figure 0.15: Overlay of simulation results onto experimental results for the case of $E^{Eff} = 0.95$ and d = 5 mm, showing the influence of crack misalignment. In (a) the simulation is perfectly centered between the inclusions, but the actual crack is misaligned by about 300 microns, so the resultant behaviors are different. Once the simulation is adjusted off-center in (b) however, simulation and experiment match one another.

It should also be noted that there are no experimental data points present for isotropic inclusions of larger radius ($E^{Eff} < 0.83$ or for any anisotropic inclusions. This is due to challenges that arose from unstable crack propagation as well as deviations between the idealized surfing load condition and the experimentally applied surfing load. For inclusions of radius greater than r ≈ 0.75mm ($E^{Eff} = 0.83$), cracks have a greater tendency to rapidly and unstably propagate between successive inclusions. In the case of simulations, this is not an issue, as it is relatively straightforward to have the load travel steadily with the tip of the crack. However, the experimental setup relies on steady propagation of the crack to prevent buildup of tensile load as the sample travels along the rail. As a result, samples with inclusions of radius greater

than r ≈ 0.75mm exhibited significant pinning at the first inclusion encountered followed by sudden rapid propagation through the specimen that could not readily be analyzed.

This pinning behavior followed by rapid propagation was also seen in nearly all anisotropic samples, as the presence of stress concentrators further increased the tendency for unstable crack propagation. As a result, no reliable toughness measurements were able to be made, and the anisotropic specimens could only be characterized based on crack path analysis after fracture. Even so, when the crack paths of the different anisotropic specimens are analyzed, differences are noticeable between different inclusion orientations. In the case of left-facing inclusions, the crack enters and exits through the circular arc region of the inclusion, as predicted by the simulation, which would indicate a toughening effect similar to that of isotropic circles. Alternatively, the crack path of the specimens with right-facing heterogneities follows successive stress concentrators, which would indicate a lower toughness behavior, as predicted by simulations.

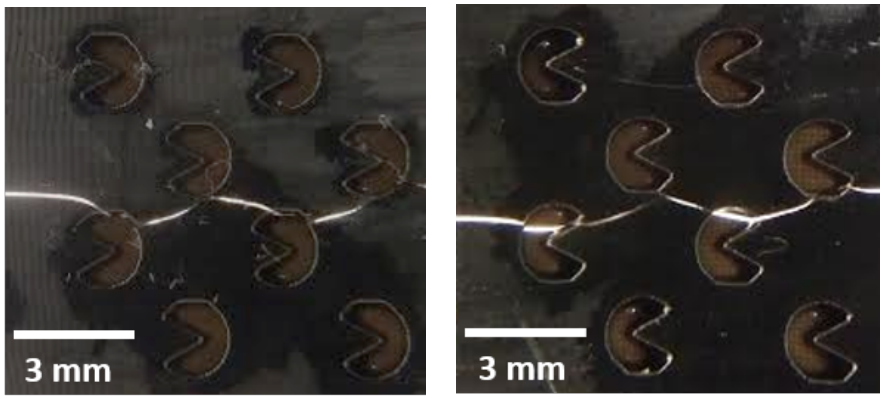

(a) Left Facing (higher toughness) (b) Right Facing (lower toughness)

Figure 0.16: Images of anisotropic composites $E^{Eff} = 0.82$ showing the difference in crack behavior between (a) left- and (b) right- facing heterogeneities. In both cases, crack propagation was from left to right.

0.6 Outlook

0.6.1 Experimental Limitations

Although experiments were able to demonstrate composite toughening for some cases of isotropic heterogneities, overall, the composite design space that could be explored was relatively limited. This was due not only to the previously discussed unstable propagation behavior, but also due to large variability seen in the measured mechanical response of the photopolymer specimens. It is suspected that this

variation is not the result of the testing technique, but is rather due to limitations associated with the material itself. The PR48 photopolymer was a well-suited model material because of its brittle nature, good shape retention, and compatibility with the Ember DLP printer used for sample fabrication. However, with PR48 as well as all other acrylate photopolymers, some issues arise with material stability. Many of the acrylate photopolymer systems used in stereolithography and digital light processing are based on photochemistry originally developed for mask lithography of silicon wafers. These systems have exceptionally good definition and shape retention, but they were not designed for long term use or stability, particularly in environments containing UV light and oxygen. This is demonstrated in a study by Chiantore et al. on the photodegradation of acrylic and methacrylic polymers.[50] The study explored the degradation behavior of four different polymers: poly(methyl acrylate), poly(ethyl methacrylate), poly(ethyl acrylate), and poly(butyl methacrylate). Each polymer was subjected to both UV radiation and oxygen, and the extent of degradation was characterized by the extent of volatilization of low molecular weight groups as well as the oxidative cross linking of side chains. The general trends in decomposition behavior were that methacrylic polymers were more stable than acrylics, and polymers with smaller side groups tended to be more stable, e.g., poly(butyl methacrylate) exhibited the most rapid and extensive decomposition as well as the most cross-linking of side chains.[50] Although to date, no quantative degradation analyses of 3D printed polymers have been published, the trends in the investigation by Chiantore et al. are highly unfavorable for many 3D printing photopolymers, including the PR48 used in this study. These polymers tend to be acrylates with very large side chain groups to minimize the amount of network formation needed achieve freestanding solid.[7] This implies that these polymers are likely to be very succeptible to degradation in environments containing oxygen and UV light, which includes the environment in which surfing load tests were performed. This degradation can lead to embrittlement and significantly higher variability in mechanical properties, which makes direct comparison of strengths and toughnesses much more difficult. Additionally, cleaning and drying processes that expose the polymer to solvents can further lead to nonuniform embrittlement, which further increases mechanical variability. Such limitations made detailed mechanical analysis of composite structures made from PR48 especially challenging.

0.7 The Potential of Anisotropic Heterogenities

Up to this point in the investigation, anisotropy has only demonstrated the potential to achieve comparable toughness to isotropic inclusions under certain loading conditions. However, the real potential of anistropic inclusions lies in the case of biased or directional loads. Both numerical simulations and crack path evaluation show strong evidence that in one particular direction, anistropic inclusions behave very similarly to isotropic ones. Additionally, numerical simulations showed that anisotropic inclusions could demonstrate similar toughness to isotropic ones at smaller volume fractions, as the removal of one portion of the circle significantly reduces the total volume occupied by the inclusion. This reduction in volume at the expense of toughness in one direction is where the potential of these anisotropic inclusions lies. If a composite is expected to experience a biased or directional load, anisotropic inclusions could be used to toughen the composite in that particular direction with significantly less impact on bulk properties. The achievable limit of this type of toughening is dictated by processing though, so the dilute limit of toughness attainable without significant modulus reduction is dictated by the resolution at which structures can be fabricated without loss of fidelity. Even so, this type of anisotropic composite reinforcement could, make it much easier to toughen extremely stiff materials with a more compliant phase without creating a dramatic loss in stiffness which would be extremely desirable in many different applications where ceramics or brittle metals are traditionally used, such as engine environments or structural applications.

0.7.1 Extension to Ceramics

Given the limited chemical stability of photopolymers and the potential of anistropic toughening in systems, it is logical explore the extension of these designs into ceramics systems. However, extending the surfing load configuration into ceramics proved infeasible, not because of challenges with sample fabrication, but because if difficulties with surfing load test design. For the experimental implementation of the surfing load, a diverging rail is used to prescribe the crack opening displacement to the sample, as shown in Figure 0.2. The magnitude of the divergence on this rail is chosen based on the stiffness and fracture toughenss of the material being fractured. For the case of the brittle photopolymer PR48, the toughness of the photopolymer, 1-2 MPa$\sqrt{\text{m}}$, is comparable to that of many ceramics and glasses, but the stiffness of the photopolymer, around 740 MPa, is lower than most ceramics and glasses by at least a factor of 100. This means that in order to test ceramics using the surfing

load, a rail with a diverging width about 100 times smaller than the current design would be needed. For the PR48 photopolymer, the rail used was made of 6061 aluminum (McMaster Carr, Elhurst, IL), and the divergence used was on the of 1-2 mm. Therefore, to test ceramics using this same design, a rail would need to a divergence on the order of tens of microns with very tight tolerances, and almost all slip in the pins and bearings used to move the sample along the rail would have to be removed. For this reason, the surfing load proved infeasible for use on ceramics, and other characterization techniques were explored in Chapters 4 and 5.

0.8 Summary

To gain a better understanding of the effects of designed anisotropy on crack propagation, we explored parameterized composite structures under stable crack growth conditions with full-field displacement measurement techniques. The composites were printed using PR48 photopolymer and stable crack growth was achieved using a novel controlled propagation technique known as the surfing load. Toughness analysis was achieved through the use of J-integrals performed on displacement fields obtained using the grid method on uniform grid patterns composed of photopolymer and powder to minimize their impact on fracture behavior. Composites were parameterized by fixing inclusion arrangement to be a staggered pattern of circular inclusions, and the stiffness of the structures were varied by changing the radius of these inclusions. Rather than using a second material, elastic and toughness contrast were tailored between inclusion and composite by changing the thickness of the specimen in different regions to change the relative stiffness and toughness. Finally, anisotropy was introduced into the structure by cutting an isosceles right triangle out of the circular inclusion to make an incomplete circle with stress concentrators on one side.

Numerical analysis showed that the introduction of more compliant heterogeneities increased composite toughness marginally at first, and then much more significantly, as the the elastic contrast from the inclusions became significant enough to produce crack-inclusion interaction. The initial marginal increase was related to crack deflection behavior, where the crack would be attracted to inclusions, altering its propagation trajectory, but no actual pinning would occur. Once inclusions increased enough in size to create sufficient elastic contrast, the crack would be pinned in the inclusions, causing a significant increase in toughness. This toughness improvement due to elastic contrast was seen both in numerical simulations as well as analogous experiment, though no toughening through crack deflection was observed

in experiment due to the sensitivity of the deflection behavior to small changes in crack position. In the case of anisotropy, the presence of stress concentrators on one side of the circular arc of the specimen reduced the toughness improvement from elastic contrast pinning in one direction, but the opposite direction exhibited similar toughening to the isotropic case, albeit at a smaller inclusion phase fraction. Experimental analysis of large inclusions and anisotropic inclusions was limited due to unstable growth arising from a combination of the heterogeneous structure and the limitations of the experimental surfing load condition.

Although no quantitative analysis could be performed, the potential of anisotropy is still apparent for cases of biased or directional loading. Because toughening is governed by the elastic contrast and local structure of the interface, it is possible to make anisotropic inclusions structures that mitigate crack propagation similarly to isotropic ones as long as loading is biased in one particular direction. The benefit of the anisotropy in this case is that the anisotropic heterogeneities use a significantly smaller volume fraction of inclusion phase, making them much more favorable for retention of bulk matrix properties, which is desirable in structural ceramics or ceramic systems designed for engine environments.

REFERENCES

[1] N. R. Brodnik, C. J. Hsueh, and M. T. Johnson. A nonconstraining templated powder grid for measurement of strain. *Strain*, 2018. ISSN 14751305. doi: 10.1111/str.12273.

[2] N. R. Brodnik, C.-J. Hsueh, K. Bhattacharya, B. Bourdin, K.T. Faber, and G. Ravichandran. Guiding and trapping cracks with compliant inclusions for enhancing toughness of brittle composite materials. *Submitted to Journal of Applied Mechanics*, 2019.

[3] M Y He and J W Hutchinson. Crack Deflection at an Interface Between Dissimilar Elastic-Materials. *Int J Solids Struct*, 25(9):1053–1067, 1989.

[4] Brian R. Lawn. *Fracture of brittle solids*. Cambridge University Press, 1993. ISBN 9780511623127.

[5] M. Z. Hossain, C. J. Hsueh, B. Bourdin, and K. Bhattacharya. Effective toughness of heterogeneous media. *Journal of the Mechanics and Physics of Solids*, 71(1):15–32, 2014. ISSN 00225096. doi: 10.1016/j.jmps.2014.06.002. URL http://dx.doi.org/10.1016/j.jmps.2014.06.002.

[6] C.-J. Hsueh. Effective toughness of heterogeneous materials. *PhD Thesis, California Institute of Technology*, 2017.

[7] AutoDesk. Autodesk Standard Clear PR48 Formulation. https://cdn-standard3.discourse.org/uploads/autodesk/original/1X/1b755fa09bb75aae7395f2ffccd444c68b06f3ba.pdf, 2017. [Online; accessed 10-June-2017].

[8] K.T. Faber and A.G. Evans. Crack deflection processes—I. Theory. *Acta Metallurgica*, 31(4):565–576, apr 1983. ISSN 0001-6160. doi: 10.1016/0001-6160(83)90046-9. URL https://www.sciencedirect.com/science/article/pii/0001616083900469.

[9] Neng Wang and Shuman Xia. Cohesive fracture of elastically heterogeneous materials: An integrative modeling and experimental study. *Journal of the Mechanics and Physics of Solids*, 98:87–105, jan 2017. ISSN 0022-5096. doi: 10.1016/J.JMPS.2016.09.004. URL https://www.sciencedirect.com/science/article/pii/S0022509616303313.

[10] Owen Smithyman. Ember Standard Clear - Mechanical Properties. http://forum.ember.autodesk.com/t/ember-standard-clear-mechanical-properties/71/2, 2016. [Online; accessed 10-June-2017].

[11] H. Moulinec and P. Suquet. A fft-based numerical method for computing the mechanical properties of composites from images of their microstructures. In *IUTAM Symposium on Microstructure-Property Interactions in Composite Materials*, pages 235–246. Springer, 1995.

[12] H. Moulinec and P. Suquet. A numerical method for computing the overall response of nonlinear composites with complex microstructure. *Computer methods in applied mechanics and engineering*, 157(1-2):69–94, 1998.

[13] J.C. Michel, H. Moulinec, and P. Suquet. A computational scheme for linear and non-linear composites with arbitrary phase contrast. *International Journal for Numerical Methods in Engineering*, 52(1-2):139–160, 2001.

[14] James R Rice. Mathematical Analysis in the Mechanics of Fracture. Technical report, 1968. URL http://esag.harvard.edu/rice/018{_}Rice{_}MathAnalMechFract{_}68.pdf.

[15] Michel Grédiac. The use of full-field measurement methods in composite material characterization: interest and limitations. *Composites Part A: Applied Science and Manufacturing*, 35(7-8):751–761, jul 2004. ISSN 1359835X. doi: 10.1016/j.compositesa.2004.01.019. URL http://linkinghub.elsevier.com/retrieve/pii/S1359835X04000260.

[16] Frank C Demarest. High-resolution, high-speed, low data age uncertainty, heterodyne displacement measuring interferometer electronics. *Measurement Science and Technology*, 9(7):1024–1030, jul 1998. ISSN 0957-0233. doi: 10.1088/0957-0233/9/7/003. URL http://stacks.iop.org/0957-0233/9/i=7/a=003?key=crossref.7a9b270bed78db7ab79a4909ced2fcec.

[17] Hareesh V. Tippur, Sridhar Krishnaswamy, and Ares J. Rosakis. Optical mapping of crack tip deformations using the methods of transmission and reflection coherent gradient sensing: a study of crack tip K-dominance. *International Journal of Fracture*, 52(2):91–117, 1991. ISSN 0376-9429. doi: 10.1007/bf00032372. URL https://link.springer.com/article/10.1007{\%}2FBF00032372?LI=true.

[18] Vasco Ronchi. Forty Years of History of a Grating Interferometer. *Applied Optics*, 3(4):437, apr 1964. ISSN 0003-6935. doi: 10.1364/AO.3.000437. URL https://www.osapublishing.org/abstract.cfm?URI=ao-3-4-437.

[19] H. Lee and S. Krishnaswamy. A compact polariscope/shearing interferometer for mapping stress fields in bimaterial systems. *Experimental Mechanics*, 36 (4):404–411, dec 1996. ISSN 0014-4851. doi: 10.1007/BF02328585. URL http://link.springer.com/10.1007/BF02328585.

[20] T. C. Chu, W. F. Ranson, and M. A. Sutton. Applications of digital-image-correlation techniques to experimental mechanics. *Experimental Mechanics*, 25(3):232–244, sep 1985. ISSN 0014-4851. doi: 10.1007/BF02325092. URL http://link.springer.com/10.1007/BF02325092.

[21] H. A. Bruck, S. R. McNeill, M. A. Sutton, and W. H. Peters. Digital image correlation using Newton-Raphson method of partial differential correction. *Experimental Mechanics*, 29(3):261–267, sep 1989. ISSN 0014-4851. doi: 10.1007/BF02321405. URL http://link.springer.com/10.1007/BF02321405.

[22] Bing Pan, Kemao Qian, Huimin Xie, and Anand Asundi. Two-dimensional digital image correlation for in-plane displacement and strain measurement: a review. *Measurement Science and Technology*, 20(6):062001, jun 2009. ISSN 0957-0233. doi: 10.1088/0957-0233/20/6/062001. URL http://stacks.iop.org/0957-0233/20/i=6/a=062001?key=crossref.37cf26a6947e54eb5498e67742a4e2ad.

[23] J. C. Wyant. Double Frequency Grating Lateral Shear Interferometer. *Applied Optics*, 12(9):2057, sep 1973. ISSN 0003-6935. doi: 10.1364/AO.12.002057. URL https://www.osapublishing.org/abstract.cfm?URI=ao-12-9-2057.

[24] F. P. Chiang and A. Asundi. White light speckle method of experimental strain analysis. *Applied Optics*, 18(4):409, feb 1979. ISSN 0003-6935. doi: 10.1364/AO.18.000409. URL https://www.osapublishing.org/abstract.cfm?URI=ao-18-4-409.

[25] MA Sutton, WJ Wolters, WH Peters, WF Ranson, and SR McNeill. Determination of displacements using an improved digital correlation method. *Image and Vision Computing*, 1(3):133–139, aug 1983. ISSN 02628856. doi: 10.1016/0262-8856(83)90064-1. URL http://linkinghub.elsevier.com/retrieve/pii/0262885683900641.

[26] Sven Bossuyt. Optimized Patterns for Digital Image Correlation. pages 239–248. Springer, New York, NY, 2013. doi: 10.1007/978-1-4614-4235-6_34. URL http://link.springer.com/10.1007/978-1-4614-4235-6{_}34.

[27] G.F. Bomarito, J.D. Hochhalter, T.J. Ruggles, and A.H. Cannon. Increasing accuracy and precision of digital image correlation through pattern optimization. *Optics and Lasers in Engineering*, 91:73–85, apr 2017. ISSN 01438166. doi: 10.1016/j.optlaseng.2016.11.005. URL http://linkinghub.elsevier.com/retrieve/pii/S0143816616304110.

[28] M. Grédiac, F. Sur, and B. Blaysat. The Grid Method for In-plane Displacement and Strain Measurement: A Review and Analysis. *Strain*, 52(3):205–243, jun 2016. ISSN 00392103. doi: 10.1111/str.12182. URL http://doi.wiley.com/10.1111/str.12182.

[29] J Tracy, A Waas, and S Daly. Experimental assessment of toughness in ceramic matrix composites using the j-integral with digital image correlation part i: methodology and validation. *Journal of Materials Science*, 50(13):4646–4658, 2015.

[30] Vincent J. Parks. The grid method. *Experimental Mechanics*, 9(7):27–33, jul 1969. ISSN 0014-4851. doi: 10.1007/BF02325141. URL http://link.springer.com/10.1007/BF02325141.

[31] Vincent J. Parks. Strain Measurement Using Grids. *Optical Engineering*, 21(4):633–639, aug 1982. ISSN 0091-3286. doi: 10.1117/12.7972958. URL http://opticalengineering.spiedigitallibrary.org/article.aspx?doi=10.1117/12.7972958.

[32] R Sowerby, E Chu, and J L Duncan. Determination of large strains in metalforming. *The Journal of Strain Analysis for Engineering Design*, 17(2):95–101, apr 1982. ISSN 0309-3247. doi: 10.1243/03093247V172095. URL http://journals.sagepub.com/doi/10.1243/03093247V172095.

[33] D. W. Manthey and D. Lee. Recent developments in a vision-based surface strain measurement system. *JOM*, 47(7):46–49, jul 1995. ISSN 1047-4838. doi: 10.1007/BF03221231. URL http://link.springer.com/10.1007/BF03221231.

[34] Y. Morimoto, Y. Seguchi, and T. Higashi. Strain analysis by mismatch moire method and grid method using Fourier transform. *Computational Mechanics*, 6(1):1–10, 1990. ISSN 0178-7675. doi: 10.1007/BF00373795. URL http://link.springer.com/10.1007/BF00373795.

[35] Shengnan Sun, Michel Grédiac, Evelyne Toussaint, Jean-Denis Mathias, and Narimane Mati-Baouche. Applying a Full-Field Measurement Technique to Characterize the Mechanical Response of a Sunflower-Based Biocomposite. *Experimental Mechanics*, 55(5):917–934, jun 2015. ISSN 0014-4851. doi: 10.1007/s11340-015-9988-1. URL http://link.springer.com/10.1007/s11340-015-9988-1.

[36] M.J. Hÿtch, E. Snoeck, and R. Kilaas. Quantitative measurement of displacement and strain fields from HREM micrographs. *Ultramicroscopy*, 74(3):131–146, aug 1998. ISSN 03043991. doi: 10.1016/S0304-3991(98)00035-7. URL http://linkinghub.elsevier.com/retrieve/pii/S0304399198000357.

[37] M.J. Hÿtch and T. Plamann. Imaging conditions for reliable measurement of displacement and strain in high-resolution electron microscopy. *Ultramicroscopy*, 87(4):199–212, may 2001. ISSN 03043991. doi: 10.1016/S0304-3991(00)00099-1. URL http://linkinghub.elsevier.com/retrieve/pii/S0304399100000991.

[38] Huimin Xie, Satoshi Kishimoto, Anand Asundi, Chai Gin Boay, Norio Shinya, Jin Yu, and Bryan K A Ngoi. In-plane deformation measurement using the atomic force microscope moiré method. *Nanotechnology*, 11(1):24–29, mar 2000. ISSN 0957-4484. doi: 10.1088/0957-

4484/11/1/305. URL http://stacks.iop.org/0957-4484/11/i=1/a=305?key=crossref.3625f95a7f67d2849060d7451d6024fe.

[39] Huimin Xie, Zhanwei Liu, Daining Fang, Fulong Dai, Hongjun Gao, and Yapu Zhao. A study on the digital nano-moiré method and its phase shifting technique. *Measurement Science and Technology*, 15(9): 1716–1721, sep 2004. ISSN 0957-0233. doi: 10.1088/0957-0233/15/9/007. URL http://stacks.iop.org/0957-0233/15/i=9/a=007?key=crossref.e2b1ff934d20c903ad76a862dc315266.

[40] J.-L. Piro and M. Grediac. PRODUCING AND TRANSFERRING LOW-SPATIAL-FREQUENCY GRIDS FOR MEASURING DISPLACEMENT FIELDS WITH MOIRE AND GRID METHODS. *Experimental Techniques*, 28(4):23–26, jul 2004. ISSN 0732-8818. doi: 10.1111/j.1747-1567.2004.tb00173.x. URL http://doi.wiley.com/10.1111/j.1747-1567.2004.tb00173.x.

[41] Rostand Moutou Pitti, Claudiu Badulescu, and Michel Grédiac. Characterization of a cracked specimen with full-field measurements: direct determination of the crack tip and energy release rate calculation. *International Journal of Fracture*, 187(1):109–121, may 2014. ISSN 0376-9429. doi: 10.1007/s10704-013-9921-5. URL http://link.springer.com/10.1007/s10704-013-9921-5.

[42] B Ribbens. Development and validation of a time-domain fringe pattern analysis technique for the measurement of object shape and deformation. *PhD Thesis, Vrije Universistat Brussel and Universitat Antwerpen*, 2015.

[43] Lorna J Gibson and Michael F Ashby. *Cellular Solids: Structure and Properties - Lorna J. Gibson, Michael F. Ashby - Google Books*. Cambridge University Press, 2 edition, 1997. ISBN 0 521 49911 9. URL https://books.google.com/books?hl=en{\&}lr={\&}id=rzVIBAAAQBAJ{\&}oi=fnd{\&}pg=PR7{\&}dq=gibson+ashby+cellular+solids+structure+and+properties+citation{\&}ots=gw5x9{_}7xBU{\&}sig=JBe66HXSx7{_}2pEbPAvsWC6rE0Fw{\#}v=onepage{\&}q{\&}f=false.

[44] Baikowski. Baikowski Malakoff HP DPM. http://www.baikowski.com/products, 2017. [Online; accessed 10-June-2017].

[45] G.A. Francfort and J.-J. Marigo. Revisiting brittle fracture as an energy minimization problem. *Journal of the Mechanics and Physics of Solids*, 46 (8):1319–1342, aug 1998. ISSN 0022-5096. doi: 10.1016/S0022-5096(98)00034-9. URL https://www.sciencedirect.com/science/article/pii/S0022509698000349.

[46] B. Bourdin, G.A. Francfort, and J-J. Marigo. Numerical experiments in revisited brittle fracture. *Journal of the Mechanics and Physics of Solids*, 48(4):797–826, apr 2000. ISSN 0022-5096. doi: 10.1016/S0022-5096(99)

00028-9. URL https://www.sciencedirect.com/science/article/pii/S0022509699000289.

[47] Blaise Bourdin, Gilles A. Francfort, and Jean-Jacques Marigo. The Variational Approach to Fracture. *Journal of Elasticity*, 91(1-3):5–148, apr 2008. ISSN 0374-3535. doi: 10.1007/s10659-007-9107-3. URL http://link.springer.com/10.1007/s10659-007-9107-3.

[48] G.P. Cherepanov. Crack propagation in continuous media: PMM vol. 31, no. 3, 1967, pp. 476–488. *Journal of Applied Mathematics and Mechanics*, 31(3):503–512, jan 1967. ISSN 0021-8928. doi: 10.1016/0021-8928(67)90034-2. URL https://www.sciencedirect.com/science/article/pii/0021892867900342.

[49] A. A. Griffith. The Phenomena of Rupture and Flow in Solids. *Philosophical Transactions of the Royal Society A: Mathematical, Physical and Engineering Sciences*, 221(582-593):163–198, jan 1921. ISSN 1364-503X. doi: 10.1098/rsta.1921.0006. URL http://rsta.royalsocietypublishing.org/cgi/doi/10.1098/rsta.1921.0006.

[50] O. Chiantore, L. Trossarelli, and M. Lazzari. Photooxidative degradation of acrylic and methacrylic polymers. *Polymer*, 41(5):1657–1668, mar 2000. ISSN 00323861. doi: 10.1016/S0032-3861(99)00349-3. URL http://linkinghub.elsevier.com/retrieve/pii/S0032386199003493.